Robust Passivity-based Control Integrated with UDE Strategy for Grid-Tied Inverter

Umit Akin Uslu[1,*], Mehmet Timur Aydemir[2]
[1]*Department of Electrical and Electronics Engineering, Alanya Alaaddin Keykubat University, Alanya/Antalya 07425, Turkiye*
[2]*Department of Electrical and Electronics Engineering, Kadir Has University, Istanbul 34084, Turkiye*
[*]*akin.uslu@alanya.edu.tr; timur.aydemir@khas.edu.tr*

***Abstract*—Uncertainties caused by parametric variations, external disturbances, and modelling errors of grid-tied inverters (GTI) make it challenging to select a proper gain for the desired controller. The performance of conventional passivity-based controller (PBC), which depends on a strictly accurate mathematical model of the system, is seriously deteriorated due to having poor robustness against parametric uncertainties and disturbances. To this end, this paper presents an improved passivity-based controller scheme assisted with uncertainty and disturbance estimator (UDE) for GTI. The UDE that has been adopted into the proposed UDE-PBC loops is used to simultaneously estimate uncertainties, which can achieve robust control and provide zero steady-state error. Moreover, the proposed UDE-PBC enables a two-degree-of-freedom (2DOF) control structure; one dedicated for disturbance rejection and the other for closed-loop tracking response of GTI system. The effectiveness of the proposed control scheme has been verified in an experimental prototype of 2 kW and compared with the base controllers in terms of robustness and transient response.**

***Index Terms*—Grid-tied inverter (GTI); Interconnection and damping assignment (IDA); Passivity-based control (PBC); Uncertainty and disturbance estimator (UDE); Port-controlled Hamiltonian (PCH).**

I. INTRODUCTION

The grid-tied inverter (GTI), which is an integral part of distributed power generation systems, is used for power conversion between DC power sources and the power grid. GTI have been employed in various industrial applications such as interface of renewable energy systems with uninterruptable power supplies (UPS), microgrid, hybrid electric transportation, HVDC, etc. [1]–[4].

Numerous control methods for grid-tied power converters have been proposed, such as deadbeat control [5], repetitive control [6], passivity-based control [7], resonant control [8], [9], model predictive control [10], backstepping control [11], and passivity-based control (PBC) [12], [13].

Among the aforementioned nonlinear control techniques, PBC has the simplest structure to implement the process and the strongest robustness against external perturbations. PBC was first introduced by Ortega *et al*. [14]–[16]. It is based on the energy conservation properties of the system under consideration. The PBC reshapes the dissipated energy of the system by injecting external matrices to make the closed-loop system passive. PBC has emerged as a favourable control scheme for power electronics used in many industry applications, such as energy storage systems (ESSs) [17], railway systems [18], STATCOM [19], and inductive power transfer (IPT) [20].

In [17], a hierarchical control method based on port-controlled Hamiltonian (PCH) model of hybrid energy storage system (HESS) was proposed. In [18], PBC has been studied for multilevel railway power conditioning (RPC) to protect parametric mismatches between the controller and the real values. In this way, the deterioration of control performance has been avoided.

In [19], a robust PBC approach was studied for STATCOM. Additionally, disturbance observer (DO) has been used to estimate parametric uncertainties and disturbances. In [20], a novel IDA-PBC strategy was suggested for DC microgrids that includes an energy storage system (ESS). To improve the steady-state performance, the proposed method has been supported by integral action.

Since direct measurement of uncertainties and disturbances cannot be frequent, a new class of control approaches based on the disturbance observer has been proposed for robustness concerns in recent decades. The key idea behind this strategy is to compensate the influence of the disturbance with the estimated disturbance from measurable states. During the recent decades, several approaches related to estimation-based techniques have been researched and applied to GTI. For example, active disturbance rejection control (ADRC) [21], extended state observer (ESO)-based control [22], disturbance observer-based (DOB) control [23], and uncertainty and disturbance estimator (UDE)-based control [24]–[28].

Recently, interest in UDE-based control method has increased due to its simplicity in control design, and good abilities of providing robustness without the requirements of an accurate model of uncertainty and disturbances. UDE-based control benefits from an appropriate first-order low-pass filter with an acceptable bandwidth that estimates and attenuates the modelling uncertainties and lumped disturbances at the same time. Analysis and design of UDE-based control was first introduced in [24] and has been further

Manuscript received 8 April, 2025; accepted 27 June, 2025.

elaborated in [25]. Indirect control of grid side current has been achieved by measuring the inverter side current for LCL filtered inverter [26]. Besides, a harmonic series of parametric uncertainties of the inverter were adopted in UDE-based control. With the help of time-delay infinite impulse response filter, a novel UDE-based control approach has been adopted for the constant voltage and constant frequency operation of the inverter [27]. In [28], UDE-based control has been used for LCCL filtered grid-tied inverter. Series damping resistances added to the parallel capacitors allow study for a first-order system and indirect grid side current control has been achieved by using current between two capacitor branches.

The main objectives of this paper are as follows. At first, the port-controlled Hamiltonian model of GTI is constructed in a state-space form, and the proposed controller is designed using the interconnection and damping assignment (IDA) approach, to eliminate coupling terms between current dynamics under the synchronous reference frame (SRF). Also, independent dynamics can be established between grid currents and DC link voltage via the interconnection matrix, allowing forming a unique controller design. Then, the UDE filter is designed with appropriate bandwidth and inserted into the feed forward channel of the proposed controller to attenuate the disturbance effect. Control parameters can be designed simply to track the bandwidth and lumped disturbance bandwidth separately, utilizing the proposed controller's two degrees of freedom structure. Asymptotic stability analysis is provided in the Lyapunov sense of the controlled system with the UDE-PBC controller. In addition, quite a simple systematic procedure of tuning algorithm was described. The effectiveness of the proposed UDE-PBC scheme is verified on a 2 kW down scale prototype of the GTI system, using comparative experimental studies. Compared to classical control methods, the UDE-PBC strategy offers high robustness against parametric variations and good transient response.

The rest of this paper is organised as follows. The mathematical model of the GTI with uncertainties and disturbances is first derived for the proposed control method in Section II. In Section III, theoretical and stability analysis of the proposed UDE-PBC strategy is elaborated in detail. Sections IV and V evaluate the validity of the proposed UDE PBC strategy with simulation and experimental results, respectively. Finally, the conclusion remarks are summarised in Section VI.

II. MATHEMATICAL MODEL OF GTI

A. Dynamic System Model

Figure 1 shows power circuit of the three-phase grid-tied inverter (GTI) system under consideration. The converter is connected to the grid by a filter. The filter has an inductance of L and an equivalent resistance of r. The DC link capacitor between the converter terminals is C_{dc}.

The current dynamics of the grid in the synchronous rotating reference frame (SRF) can be represented as follows:

$$L\frac{dI_d}{dt} = -ri_d + \omega L i_q + u_d - v_{gd}, \tag{1}$$

$$L\frac{dI_q}{dt} = -ri_q - \omega L i_d + u_q - v_{gq}. \tag{2}$$

In these equations, u_d and u_q are the control functions, v_{gd} and v_{gq} are the grid voltages, i_d, and i_q are the grid currents. ω is the grid angular frequency and it is obtained using the phase-locked loop (PLL) scheme.

GTI regulates the DC link voltage to balance the power between injected active power on the DC side and output power produced on the grid side. Dynamic equation of the DC link voltage in terms of the total instantaneous power of the converter can be expressed as follows

$$C_{dc}\frac{dV_{dc}}{dt} = \frac{1}{V_{dc}}\left[P_{dc} - \frac{V_{dc}^{\ 2}}{R_{sw}} - \left(\underbrace{P_g + P_R + P_L}_{P_t}\right)\right], \tag{3}$$

where V_{DC} and I_{dc} are the DC link capacitor voltage and pulsating current, respectively, which they form external DC power $P_{dc} = V_{dc}I_{dc}$, P_{in} is the injected power of converter DC side, which is equal to AC side terminal power P_t, R_{sw} represents the equivalent switching loss of the GTI, P_R and P_L are power losses of resistor and inductor of the grid filter, respectively, $P_g = 3/2\,(v_{gd}I_d + v_{gq}I_q)$ is equal to grid side active power. The complete power loss of the grid and inverter side is schematically represented in Fig. 2.

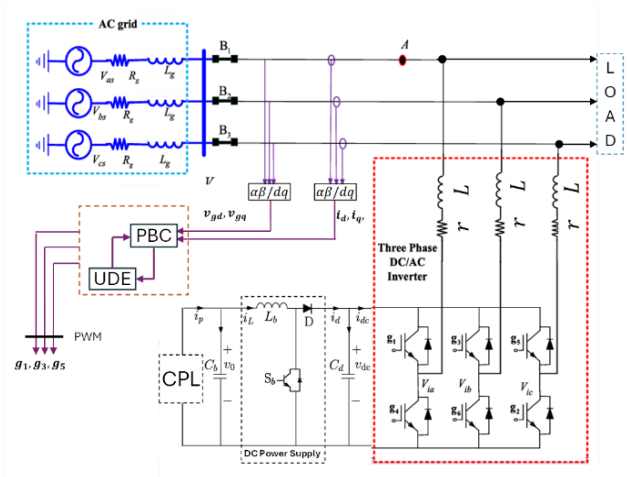

Fig. 1. Schematic diagram of the grid-tied inverter system.

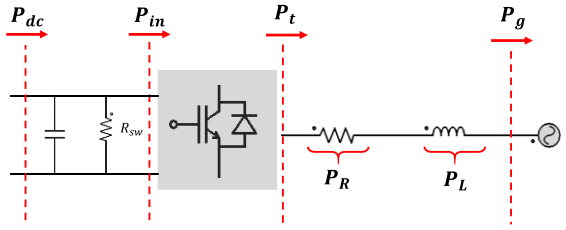

Fig. 2. Power loss diagram of GTI system.

At the steady state, I_d and I_q currents are regulated to a certain constant value, therefore P_L can be neglected. Grid-side resistive losses P_R, which are due to filter resistance can be included in the switching resistance and lumped into R_{sw}. Grid currents have a larger bandwidth than the DC link

voltage. Therefore, the dynamics of the grid currents and the DC link voltage are decoupled. Since the regulation loops of the grid currents are much faster, $I_d = I_d^*$ and $I_q = I_q^*$ can be assumed. With the help of this condition, we assume that $P_g \approx P_g^*$, where

$$P_g^* = \frac{3}{2}\left(v_{gd} I_d^* + v_{gq} I_q^*\right). \tag{4}$$

Then (3) can be reduced to

$$C\frac{dV_{dc}}{dt} = \frac{1}{V_{dc}}\left[P_{dc} - \frac{V_{dc}^2}{R_C} - P_g^*\right]. \tag{5}$$

B. Modelling Uncertainties

The rise in temperature of the filters and switches, or some other operating conditions, as well as external effects, can cause perturbation on the parameters of the system dynamics, which is difficult accurately determine. Although these disturbance effects can be neglected for practical control design, to achieve robust stability against unstructured variations, parametric uncertainties must be taken into consideration on system modelling. Moreover, unmodelled dynamics leads to further errors to control the system during run-time. Taking into account the nominal parameters and unknown external disturbances, (1)–(3) can be modified as follows:

$$\frac{di_d}{dt} = -\frac{r}{L}i_d + \omega i_q + \frac{u_d}{L} - \frac{v_{gd}}{L} + F_d, \tag{6}$$

$$\frac{di_q}{dt} = -\frac{r}{L}i_q + \omega i_d + \frac{u_q}{L} - \frac{v_{gq}}{L} + F_q, \tag{7}$$

$$\frac{dV_{dc}}{dt} = -\frac{1}{C_{dc}V_{dc}}P_g^* + F_{dc}. \tag{8}$$

In these equations, r, L and C_{dc} are nominal values of the model parameters. F_d, F_q, and F_{dc} are variables that represent lump of the model uncertainties caused by parametric variations and disturbances, and are given by:

$$F_{id} = -\frac{\Delta r}{L}i_d + \frac{\omega\Delta L}{L}i_q - \frac{\Delta v_{gd}}{L} - \frac{\Delta L}{L}\frac{di_d}{dt} + \delta_d, \tag{9}$$

$$F_{iq} = -\frac{\Delta r}{L}i_q - \frac{\omega\Delta L}{L}i_d - \frac{\Delta v_{gd}}{L} - \frac{\Delta L}{L}\frac{di_d}{dt} + \delta_q, \tag{10}$$

$$F_{dc} = -\frac{i_{dc}}{C_{dc}} - \frac{V_{dc}}{C_{dc}R_c} - \frac{\Delta C}{C_{dc}}\frac{dV_{dc}}{dt} + \delta_{dc}, \tag{11}$$

where the variables δ_d, δ_q, and δ_{dc} can be considered as unknown external disturbances acting on the system. Δr, ΔL, ΔC, and Δv_{gd}, Δv_{gq} represent unstructured uncertainties due to unmodelled dynamics.

Disturbance parameter, F_{dc} consists of constant power load P_{CPL} and resistive load currents, which can be considered as negative resistance.

C. Port-Controlled Hamiltonian Model of GTI

To apply the PBC method, the dynamic model of GTI described by (6)–(8) must be transformed into a port Hamiltonian model (pH) with the help of matrix notations [15]. Port-Hamiltonian is an important and effective modelling technique in passivity-based control design, which integrates the energy dispassivity properties of the pH model into the system and provides the stability of the system in terms of energy balancing. Then, the pH model of GTI can be expressed as follows

$$\dot{\boldsymbol{x}} = \left[\boldsymbol{J} - \boldsymbol{R}\right]\boldsymbol{Q}\boldsymbol{x} + \boldsymbol{B}\boldsymbol{u} + \boldsymbol{F}. \tag{12}$$

The state vector of the system is defined as follows

$$\boldsymbol{x} = \begin{bmatrix} I_d & I_q & V_{dc} \end{bmatrix}^T. \tag{13}$$

The Hamiltonian function $\boldsymbol{H}(\boldsymbol{x})$ represents the total energy stored in passive elements such as filter inductors and DC link capacitor of the converter, and can be selected as follows

$$\boldsymbol{H}(\boldsymbol{x}) = \frac{1}{2}\boldsymbol{x}^T\boldsymbol{Q}\boldsymbol{x}. \tag{14}$$

The matrix $\boldsymbol{Q}$ is called the inertia matrix, which is positive definite and constant

$$\boldsymbol{Q} = \begin{bmatrix} 1/L & 0 & 0 \\ 0 & 1/L & 0 \\ 0 & 0 & 1/C_{dc} \end{bmatrix}. \tag{15}$$

$\boldsymbol{J}$ is a skew-symmetric interconnection matrix and it is responsible for energy conversion of internal structure of the system

$$\boldsymbol{J} = \begin{bmatrix} 0 & \omega L & 0 \\ -\omega L & 0 & 0 \\ 0 & 0 & 0 \end{bmatrix}. \tag{16}$$

$\boldsymbol{R}$ is symmetric and positive semidefinite matrix. It is known as the damping matrix, consisting of energy dissipation elements of the inverter

$$\boldsymbol{R} = \begin{bmatrix} r & 0 & 0 \\ 0 & r & 0 \\ 0 & 0 & 0 \end{bmatrix}. \tag{17}$$

$\boldsymbol{B}$ is the transfer matrix and $\boldsymbol{u}$ is defined as the control vector that consist of exogenous inputs and grid voltage source of the system

$$\boldsymbol{B} = \begin{bmatrix} 1/L & 0 & 0 \\ 0 & 1/L & 0 \\ 0 & 0 & 1/C_{dc} \end{bmatrix}, \tag{18}$$

$$\boldsymbol{u} = \begin{bmatrix} u_d - v_{gd} & u_q - v_{gd} & P^*/V_{dc} \end{bmatrix}^T. \tag{19}$$

$\boldsymbol{F}$ corresponds to the vector of uncertainty and disturbance

$$\boldsymbol{F} = \begin{bmatrix} F_{id} & F_{iq} & F_{dc} \end{bmatrix}^T. \quad (20)$$

III. CONTROLLER DESIGN

Before applying the proposed passivity-based controller, it must be ensured that the system under investigation is strictly passive. From the dynamics given in (6)–(8), the physical structure of GTI, which is composed of the filter inductor *L*, resistor *r*, and DC link capacitor C_{dc}, makes the system inherently passive, so the proposed approach can be used to control the GTI system.

A. UDE-PBC Controller

PBC is implemented by damping injection on the dissipation part of the storage energy of the GTI system. This dissipation of energy forces the system states $\boldsymbol{x}$ to drive the desired equilibrium pont $\boldsymbol{x_d}$ with the help of the relation between control input $\boldsymbol{u}$ and the system output $\boldsymbol{y}$, such that:

$$\boldsymbol{H}\left(\boldsymbol{x}(\boldsymbol{t})\right) - \boldsymbol{H}\left(\boldsymbol{x}(\boldsymbol{0})\right) \le \int_0^t \boldsymbol{u}^T \boldsymbol{y} d\boldsymbol{\tau} - \int_0^t \boldsymbol{Q}(\boldsymbol{\tau}) d\boldsymbol{\tau}, \quad (21)$$

$$\dot{\boldsymbol{H}} \le \boldsymbol{u}^T \boldsymbol{y} - \boldsymbol{Q}(\boldsymbol{x}). \quad (22)$$

From the dissipative inequality (21), (22), if there exists a smooth positive semidefinite energy storage function $\boldsymbol{H}(\boldsymbol{x}(\boldsymbol{t}))$ and positive definite function **Q(x)**, the sum of the increment of the energy $\boldsymbol{H}(\boldsymbol{x}(\boldsymbol{t})) - \boldsymbol{H}(\boldsymbol{x}(\boldsymbol{0}))$ and dissipation of the energy $\int_0^t \boldsymbol{Q}(\boldsymbol{\tau}) d\boldsymbol{\tau}$ must be less than injected supply rate $\int_0^t \boldsymbol{u}^T \boldsymbol{y} d\boldsymbol{\tau}$. This condition proves that system is strictly passive [18], [20].

The objective of proposed control method is to determine a state feedback control law that tracks the given power references and satisfies the desired dynamics of the closed-loop system as PCH form with the following equation

$$\dot{\boldsymbol{e}} = \left[\boldsymbol{J_d} - \boldsymbol{R_d}\right] \boldsymbol{Q} \boldsymbol{e}. \quad (23)$$

Equation (16) shows that two-degree-of-freedom matrices, such as:

$$\boldsymbol{J_d} = \boldsymbol{J} + \boldsymbol{J_a}, \quad (24)$$

$$\boldsymbol{R_d} = \boldsymbol{R} + \boldsymbol{R_a}, \quad (25)$$

need to be determined. In these equations, $\boldsymbol{J_d}$ represent the desired anti-symmetrical interconnection matrix and $\boldsymbol{R_d}$ corresponds to the desired damping matrix, which is positive definite. $\boldsymbol{H_d}$ denotes the desired energy storage function with the error term $\mathrm{e} = \mathrm{x} - \mathrm{x_d}$

$$\boldsymbol{H_d} = \frac{1}{2} \boldsymbol{e}^T \boldsymbol{Q} \boldsymbol{e}, \quad (26)$$

where $x_d = [\, I_d^*, I_q^*, V_{dc}^* \,]^T$ is the desired state variable vector. To operate the converter around the desired equilibrium point, $\boldsymbol{H_d}$ should have a minimum value at the desired point of the system, i.e., $\dot{x}|_{(x=x_d)} = 0$. By keeping V_{dc}^* at DC bus voltage level, the desired state variables for the given active and reactive powers can be calculated as:

$$I_d^* = \frac{2}{3} \frac{\left[P^* v_{gd} + Q^* v_{gq}\right]}{v_{gd}^2 + v_{gq}^2}, \quad (27)$$

$$I_q^* = \frac{2}{3} \frac{\left[P^* v_{gq} + Q^* v_{gd}\right]}{v_{gd}^2 + v_{gq}^2}. \quad (28)$$

Introducing $\boldsymbol{J_a}$ and $\boldsymbol{R_a}$ matrices into the proposed control input $\boldsymbol{u}$ force the desired energy function $\boldsymbol{H_d}$ to convergence zero by $\boldsymbol{e} \to 0$, which provides the control aim. The control law for the proposed control system can be obtained from the energy matching equation by comparing the open-loop and desired closed-loop formulation of the system

$$\left(\boldsymbol{J} - \boldsymbol{R}\right)\boldsymbol{Q}\boldsymbol{x} + \boldsymbol{B}\boldsymbol{u} + \boldsymbol{F} = \left(\boldsymbol{J_d} - \boldsymbol{R_d}\right)\boldsymbol{Q}\boldsymbol{e}. \quad (29)$$

Based on (29), a candidate control input vector $\boldsymbol{u}$ can be derived as

$$\boldsymbol{u} = \boldsymbol{B}^{-1}\left(\dot{\boldsymbol{x}}_{\boldsymbol{d}} + \left(\boldsymbol{J_a} - \boldsymbol{R_a}\right)\boldsymbol{Q}\boldsymbol{x} - \left(\boldsymbol{J_d} - \boldsymbol{R_d}\right)\boldsymbol{Q}\boldsymbol{x_d} - \boldsymbol{F}\right), \quad (30)$$

where $\boldsymbol{B^{-1}}$ is the inverse of $\boldsymbol{B}$. $\boldsymbol{J_a}$, and $\boldsymbol{R_a}$ are matrices that represent the new interconnection and dissipative structure of the system, respectively. These matrices are used to synthesise the control function to reshape the energy function $\boldsymbol{H}$ to the desired one $\boldsymbol{H_d}$, and can be written as follows:

$$\boldsymbol{J_a} = \begin{bmatrix} 0 & -\omega L & 0 \\ \omega L & 0 & 0 \\ 0 & 0 & 0 \end{bmatrix}, \quad (31)$$

$$\boldsymbol{R_a} = \begin{bmatrix} r_1 & 0 & 0 \\ 0 & r_2 & 0 \\ 0 & 0 & r_3 \end{bmatrix}. \quad (32)$$

Solving (30) with respect to the control signals, the output commands are obtained as follows:

$$U_d = -\omega L i_q - r_1 i_d + r_d i_d^* + v_{gd} - L F_{id}, \quad (33)$$

$$U_q = \omega L i_d - r_2 i_q + r_d i_q^* + v_{gq} - L F_{iq}, \quad (34)$$

$$-P_{red} / V_{dc} = -r_{dc}\left(V_{dc} - V_{dc}^*\right) - C_{dc} F_{dc}. \quad (35)$$

Unfortunately, it is not possible to apply (30) since the term $\boldsymbol{F}$, which defines the lumped uncertainty and disturbance, is unknown. Based on the dynamic equation in (12), $\boldsymbol{F}$ can be represented as follows

$$\boldsymbol{F} = \dot{\boldsymbol{x}} - \left(\boldsymbol{J} - \boldsymbol{R}\right)\boldsymbol{Q}\boldsymbol{x} - \boldsymbol{B}\boldsymbol{u}. \quad (36)$$

Equation (36) shows that the uncertainty and unknown disturbance of the system can be estimated with the help of the control input and the system states. However, it cannot be used directly to derive a control function $\boldsymbol{u}$. Following the design process presented in [24], $\boldsymbol{F}$ can be accurately estimated when a low-pass filter $\boldsymbol{G_f(s)}$ with a proper bandwidth covering the spectrum of $\boldsymbol{F}$ is selected. Then, the approximation of $\boldsymbol{F}$ can be described as

$$\boldsymbol{F_d}(s) = \boldsymbol{F}\boldsymbol{G_f}(s), \tag{37}$$

where $\boldsymbol{F_d}$ is the estimated value of $\boldsymbol{F}$. $\boldsymbol{G_f}(s)$ is the low-pass filter with appropriate frequency characteristics like unity gain and zero phase shift. Replacing $\boldsymbol{F}$ with $\boldsymbol{F_d}$, the control law given in (30) is rewritten as

$$\boldsymbol{u}(s) = \boldsymbol{B}^{-1}\begin{pmatrix} s\boldsymbol{x_d} + (\boldsymbol{J_a} - \boldsymbol{R_a})\boldsymbol{Q}\boldsymbol{x}(s) - (\boldsymbol{J_d} - \boldsymbol{R_d})\boldsymbol{Q}\boldsymbol{x_d} - \\ \underbrace{-\boldsymbol{F}(s) * \boldsymbol{G_f}(s)}_{\boldsymbol{F_d}(s)} \end{pmatrix}. \tag{38}$$

Then, reformulating (37) through (38) by taking Laplace transform, $\boldsymbol{F_d}$ can be written as (39)

$$\boldsymbol{F_d}(s) = \left[s\boldsymbol{x}(s) - (\boldsymbol{J} - \boldsymbol{R})\boldsymbol{Q}\boldsymbol{x}(s) - \boldsymbol{B}\boldsymbol{u}(s)\right]\boldsymbol{G_f}(s). \tag{39}$$

By substituting (39) into (30), the proposed control law is reformulated in (41). From (41), $\boldsymbol{G_f}(s)$ and $\boldsymbol{R_f}$ matrices are given as:

$$\boldsymbol{G_f} = \left(s\boldsymbol{I_{3x3}} + \boldsymbol{R_f}\right)^{-1}\boldsymbol{R_f}, \tag{40}$$

$$\boldsymbol{u}(s) = \boldsymbol{B}^{-1}\left[\begin{pmatrix} \left(s\boldsymbol{I_{3x3}} - (\boldsymbol{J_d} - \boldsymbol{R_d})\boldsymbol{Q}\right)\boldsymbol{x_d} + \\ + \begin{pmatrix} (\boldsymbol{J_a} - \boldsymbol{R_a})\boldsymbol{Q} - \left(s\boldsymbol{I_{3x3}} - (\boldsymbol{J} - \boldsymbol{R})\boldsymbol{Q}\right)\times \\ \times \boldsymbol{G_f}(s) \end{pmatrix}\boldsymbol{x}(s) \end{pmatrix}\times\right.$$

$$\left.\times\frac{\boldsymbol{I_{3x3}}}{\boldsymbol{I_{3x3}} - \boldsymbol{G_f}(s)}\right], \tag{41}$$

$$\boldsymbol{R_f} = \begin{bmatrix} R_{fd} & 0 & 0 \\ 0 & R_{fq} & 0 \\ 0 & 0 & R_{fdc} \end{bmatrix}, \tag{42}$$

$$\boldsymbol{R_d} = \begin{bmatrix} r_d & 0 & 0 \\ 0 & r_q & 0 \\ 0 & 0 & r_{dc} \end{bmatrix}, \tag{43}$$

where $\boldsymbol{G_f}$ is low-pass filter vector and the $\boldsymbol{R_f}$ matrix consists of appropriate bandwidths R_{fd}, R_{fq}, and R_{fdc} with unity gains and zero phase shift over the spectrum of F_{id}, F_{iq}, and F_{dc} disturbance terms, respectively. Transfer function of filter vector for appropriate channel is given below

$$\boldsymbol{G_f}(s) = \boldsymbol{diag}\left(G_{fd}(s), G_{fq}(s), G_{fdc}(s)\right) = \\ = \boldsymbol{diag}\left(\frac{R_{fd}}{s + R_{fd}}, \frac{R_{fq}}{s + R_{fq}}, \frac{R_{fdc}}{s + R_{fdc}}\right). \tag{44}$$

In this manner, uncertainty and unknown disturbances are eliminated from the control law. It is clear that (41) consists of reference states, nominal parameters, known states, and filter $\boldsymbol{G_f}$. Transfer function of output commands vector for the appropriate channel is given below:

$$U_d = (sL + r)i_d^* - \omega L i_q - r_1\left(i_d - i_d^*\right) + v_{gd} - \\ -LR_{fd}F_{id} - r_d\frac{R_{fd}}{s}\left(i_d - i_d^*\right), \tag{45}$$

$$U_q = (sL + r)i_q^* - \omega L i_d - r_2\left(i_q - i_q^*\right) + v_{gq} - \\ -LR_{fq}F_{iq} - r_q\frac{R_{fq}}{s}\left(i_q - i_q^*\right), \tag{46}$$

$$-P_{red}/V_{dc} = sC_{dc}V_{dc}^* - r_{dc}\left(V_{dc} - V_{dc}^*\right) - C_{dc}R_{fdc}F_{dc} - \\ -r_{dc}\frac{R_{fdc}}{s}\left(V_{dc} - V_{dc}^*\right). \tag{47}$$

Hence, the definition of reference states and filter parameter is important in designing the proposed controller. Inaccurate estimation of the spectrum of the disturbance caused by uncertainty, deadtime due to switching, computational delay make it difficult to define filter parameters. Therefore, selecting a first-order low-pass filter, which has enough bandwidth to cover the spectrum of the lumped disturbance term, is easy for designers.

B. Closed-Loop Analysis

Applying (41) into (12) results in and taking the Laplace transforms of both sides of the equation, the passivity and filter structure of system response can be derived as follows

$$\left[s\boldsymbol{I_{3x3}} - (\boldsymbol{J_d} - \boldsymbol{R_d})\boldsymbol{Q}\right]\boldsymbol{x}(s) = \\ = \left[s\boldsymbol{I_{3x3}} - (\boldsymbol{J_d} - \boldsymbol{R_d})\boldsymbol{Q}\right]\boldsymbol{x_d}(s) + \left(1 - \boldsymbol{G_f}\right)\boldsymbol{F}(s). \tag{48}$$

To eliminate the coupling terms, the elements of the interconnection matrix $\boldsymbol{J_a}$ can be chosen as $\boldsymbol{J_a} = -\boldsymbol{J}$, which results in $\boldsymbol{J_d} = \boldsymbol{0}$.

Then, rearranging (48)

$$\boldsymbol{X}(s) = \boldsymbol{C}(s)\boldsymbol{X_d}(s) + \boldsymbol{H}(s)\boldsymbol{F}(s), \tag{49}$$

where C_{3x3} and H_{3x3} are obtained as follows:

$$\boldsymbol{C}(s) = \left(s\boldsymbol{I_{3x3}} + \boldsymbol{R_d}\boldsymbol{Q}\right)^{-1}\left(\boldsymbol{R_d}\boldsymbol{Q}\right), \tag{50}$$

$$\boldsymbol{H}(s) = \underbrace{\left(s\boldsymbol{I_{3x3}} + \boldsymbol{R_d}\boldsymbol{Q}\right)^{-1}}_{\boldsymbol{H_c}}\underbrace{\left(\boldsymbol{1} - \boldsymbol{G_f}\right)}_{\boldsymbol{H_f}}. \tag{51}$$

Derivative of $\boldsymbol{x_d}$ converges to zero and $\boldsymbol{J_d} = 0_{3x3}$ than:

$$\boldsymbol{C}(s) = \boldsymbol{diag}\left(C_d(s), C_q(s), C_{dc}(s)\right) = \\ = \boldsymbol{diag}\left(\frac{r_d}{s + r_d}, \frac{r_q}{s + r_q}, \frac{r_{dc}}{s + r_{dc}}\right), \tag{52}$$

$$H_c(s) = \boldsymbol{diag}\left(H_{cd}(s), H_{cq}(s), H_{cdc}(s)\right) = \\ = \boldsymbol{diag}\left(\frac{L}{Ls + r_d}, \frac{L}{Ls + r_q}, \frac{C_{dc}}{C_{dc}s + r_{dc}}\right), \tag{53}$$

$$\boldsymbol{H_f}(s) = \boldsymbol{diag}\left(H_{fd}(s), H_{fq}(s), H_{fdc}(s)\right) = \\ = \boldsymbol{diag}\left(\frac{s}{s + R_{fd}}, \frac{s}{s + R_{fq}}, \frac{s}{s + R_{fdc}}\right). \tag{54}$$

The closed-loop output transfer functions for each state can

be derived as follows:

$$i_d(s) = \underbrace{\frac{r_{dd}}{sL + r_{dd}}}_{C_d(s)} i_d^* + \underbrace{\frac{L}{sL + r_{dd}}}_{H_{cd}(s)} \underbrace{\frac{s}{s + R_{fd}}}_{H_{fd}(s)} F_d, \quad (55)$$

$$i_q(s) = \underbrace{\frac{r_{dq}}{sL + r_{dq}}}_{C_q(s)} i_q^* + \underbrace{\frac{L}{sL + r_{dq}}}_{H_{cq}(s)} \underbrace{\frac{s}{s + R_{fq}}}_{H_{fq}(s)} F_q, \quad (56)$$

$$V_{dc}(s) = \underbrace{\frac{r_{dc}}{sC + r_{dc}}}_{C_{dc}(s)} v_{dc}^* + \underbrace{\frac{C}{sC + r_{dc}}}_{H_{cdc}(s)} \underbrace{\frac{s}{s + R_{fdc}}}_{H_{fdc}(s)} F_{dc}. \quad (57)$$

Equation (55)–(57) shows that the closed-loop frequency response design can be made separately for reference tracking and disturbance rejection. The desired response is determined by damping matrix $\boldsymbol{R_d}$ with the set point obtained from the desired grid power. Although the damping matrix $\boldsymbol{R_d}$ is selected according to the dynamic performance of the system, e.g., convergence rate of the reference tracking, it is not sufficient to ensure the stability of the system. Equation (55)–(57) indicates that the disturbance response is determined by the $\boldsymbol{G_f}$ filter parameter $\boldsymbol{R_f}$, which achieves asymptotic disturbance rejection and is coupled with reference tracking dynamics. How to design a $\boldsymbol{G_f}$ filter has already been formulated in [25], [28]. The bilateral relation in the frequency domain between damping matrix $\boldsymbol{R_d}$ and filter parameter $\boldsymbol{R_f}$ to track the desired reference point and reject the disturbance, respectively, can be detailed as follows.

Damping matrix parameters r_d, r_q, and r_{dc} are the key factors that affect the desired tracking reference performance. Assuming that the uncertainty errors are zero in (49), the tracking error dynamics become $x(s) = C(s)x_d(s)$, where r_d/L, r_q/L, and r_{dc}/C are time constants for the step response. If $(r_d = r_q)/L \ll r_{dc}/C_{dc}$, the current controller becomes much faster than the DC link voltage controller. In this way, two loops are effectively decoupled from each other. To obtain a good estimate of uncertainty terms $\boldsymbol{F}$, $\boldsymbol{R_f}$ matrice elements R_{fd}, R_{fq}, and R_{fdc}, which define the bandwidth of each filter, should be wide enough to cover the spectrum of the lumped disturbance F_{id}, F_{iq}, and F_{dc}, respectively. Also, filter bandwidth elements $(R_{fd}, R_{fq}, R_{fdc})$ should be chosen larger than the desired tracking response to make sure that they do not influence the controller loop performance. The parameters listed in Table I are used in the subsequent analysis. To evaluate the disturbance rejection action of the proposed scheme, the matrix $\boldsymbol{H(s)}$ in (51), which defines the transfer functions between disturbance $\boldsymbol{F(s)}$ and output $\boldsymbol{X(s)}$, can be used for the analysis of the grid currents and the DC link voltage, respectively.

TABLE I. ELECTRICAL SYSTEM PARAMETERS.

Filter inductor L	6 mH
Filter resistor r	0.35 Ω
DC link capacitor C_{dc}	1 mF
Grid frequency	50 Hz
DC link voltage reference	400 V
Phase-to-neutral voltage	100 V
Switching frequency	10 kHz
Sampling frequency	10 kHz

Attenuation filter $\boldsymbol{H(s)}$ consists of series connection of high pass filter $\boldsymbol{H_f(s)}$ and low-pass filter $\boldsymbol{H_c}$. Figure 3 shows the Bode plots of the magnitude response of the considered transfer functions $\boldsymbol{H_f(s)}$, $\boldsymbol{H_c}$, and $\boldsymbol{H(s)}$, which were expanded in (55)–(57). First, fixed damping parameters (r_d, r_q, r_{dc}) are set according to the desired closed-loop response, and then filter parameters $(R_{fd}, R_{fq}, R_{fdc})$ are changed to minimize the magnitude of $\boldsymbol{H(s)}$, transfer function matrix under allowed stability requirements. As shown in Fig. 3, with the increase of $\boldsymbol{R_f}$, the magnitude of $\boldsymbol{H(s)}$ reduces considerably in the low frequency range. The operating points residing on the right side of $\boldsymbol{R_f = R_d}$ curve $\boldsymbol{(R_f > R_d)}$ show that greater disturbance attenuation can be obtained with respect to operating points residing on the left side of $\boldsymbol{R_f = R_d}$ curve $\boldsymbol{(R_f < R_d)}$. For higher frequencies $\boldsymbol{(R_f \gg R_d)}$, all the frequency responses are superimposed, which shows the behaviour of the disturbance response is equal. Consequently, lumped disturbances $\boldsymbol{F(s)}$ can be significantly attenuated in the considered low-frequency range when the proposed control law is applied.

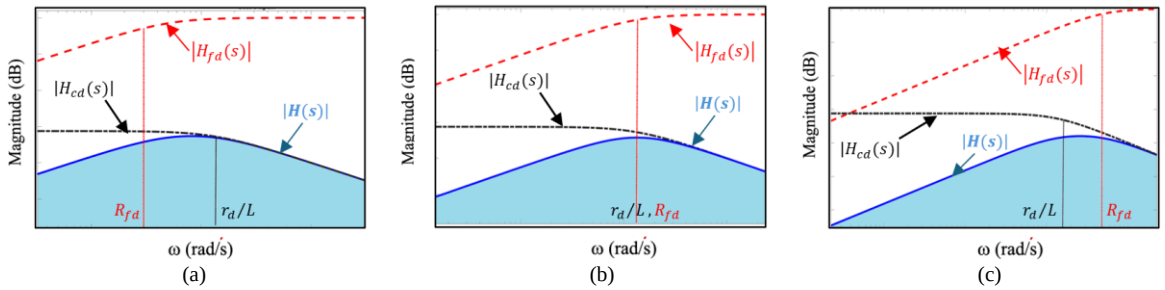

Fig. 3. Frequency response of $\boldsymbol{H(s)}$ with different $\boldsymbol{R_f}$, for certain $\boldsymbol{R_d}$: (a) $R_{fd} < r_d/L$; (b) $R_{fd} = r_d/L$; (c) $R_{fd} > r_d/L$.

Although the aforementioned discussion gives the basic approach for selecting controller and filter gain parameters, one should take some practical limitations into consideration. Sufficiently large $\boldsymbol{R_d}$ and $\boldsymbol{R_f}$ provide better tracking and estimation with smaller steady-state error. However, this causes stability problems and degrades the system noise immunity level. Another limitation can be considered as the system delay T_d caused by sampling, pulse-width modulation (PWM) updating, computation of the controller and filter, etc. T_d is the sum of one sampling period T_s for the computation and half sampling period $0.5T_s$ to update the PWM input. With PWM gain K_{pwm}, system delay can be integrated into the control loop as a first-order inertia term $G_d = K_{pwm}/(1 + sT_d)$. Closed-loop transfer function of i_d

with system delay can be derived as follows:

$$i_d(s) = G_{cd}(s) i_d^*, \tag{58}$$

$$i_q(s) = G_{cq}(s) i_q^*, \tag{59}$$

where

$$G_{c,dq}(s) = \frac{\left(P + r_{1,2} P_n P\right) G_d}{P_n\left(1 - G_{f,dq}\right) + P G_{f,dq} + r_{1,2} P_n P G_d}. \tag{60}$$

In above equation, $P(s) = 1/(sL + r)$ is the real transfer function of the plant. Complete closed-loop control diagram can be represented in Fig. 4. Figures 5 and 6 show the corresponding magnitude response of $G_{c,dq}(s)$ for various values of the control gains with taking into account the delays in the loop. Decoupled first-order structure of the transfer functions of G_{cd} (G_{cq}) make the design law easy to follow the reference value with zero steady-state error and no overshoot.

For fixed $\boldsymbol{R_f}$, tracking convergence rate increases with the increase of damping parameter $\boldsymbol{R_d}$, which constitutes the eigenvalues of the closed-loop system. On the contrary, reducing $\boldsymbol{R_d}$ makes the tracking response slow down. Selecting larger $\boldsymbol{R_d}$ values causes the dominant poles to become distant from the real axis and this leads to an oscillation. Besides, it is seen from (51) that the magnitude of $\boldsymbol{H(s)}$ reduces as $\boldsymbol{R_f}$ increases, which helps reduce high-frequency disturbance. Thus, to obtain satisfactory response, control gains need to be tuned in the range of constraints condition.

A robustness analysis has been carried out taking into account the parameter mismatch. To obtain good observation of the proposed controller, we need to deviate the grid filter parameters from their nominal values. Figure 7 shows the frequency response of G_{cd} transfer functions. Although parametric mismatches cause a small effect on the dynamic response, the proposed controller can track reference states with fast dynamic response.

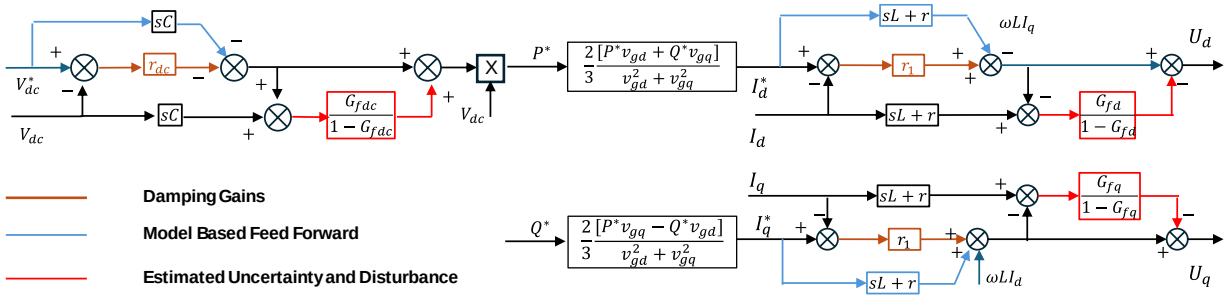

Fig. 4. Closed-loop block diagram of the proposed UDE-PBC scheme.

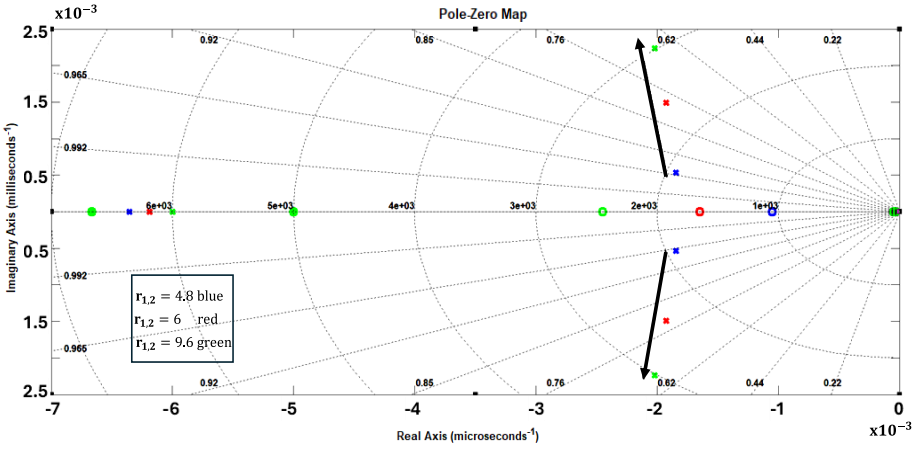

Fig. 5. Pole zero map of $G_{c,dq}(s)$ for different damping gains.

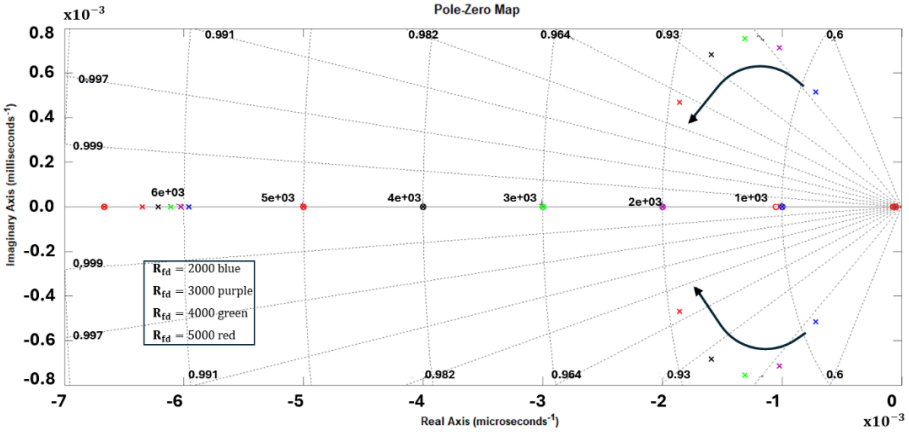

Fig. 6. Pole zero map of $G_{c,dq}(s)$ for different filter gains.

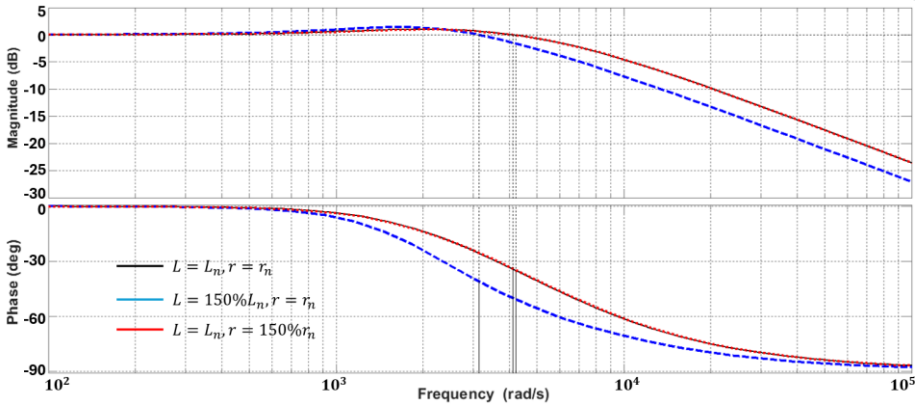

Fig. 7. Bode diagram of $G_{c,dq}(s)$ for parametric uncertainties.

IV. Simulation Results

To verify the effectiveness and performance of the proposed control strategy, some scenarios were performed through simulation taking into account dynamic response, tracking performance, robustness, and disturbance rejection. Traditional proportional-integral (PI) and PBC strategy has been selected as base controller and compared with the proposed UDE-PBC strategy. To obtain relatively fair comparison between the proposed and base controllers, their parameters are well defined in [29] to produce the same closed-loop performance. Time constant $\tau = 1/\delta\omega_n$, is the key factor that affects the desired closed-loop specifications, where δ and ω_n are damping ratio and natural angular frequency for the PI controller, respectively. To guarantee decoupled loops between current control and the DC link voltage control for stable operation, the current loop response should be faster than the voltage loop. Moreover, the minimum time constant forced by the sampling period $\tau = (2\sim3)T_s$. The coefficients K_{pi} and K_{ii} of the PI controller for the inner loop can be chosen as $K_{pi} = 2L/\tau_i$ and $K_{ii} = L\omega_{ni}^2$, with τ_i *and* ω_{ni} are the inner loop time constant and the natural frequency, respectively. The outer loop time constant τ_v should be choosen larger than the inner loop time constant τ_i, such as $\tau_v = (9\sim10)\tau_i$. Consequently, the PI parameter for the outer loop can be chosen as $K_{pv} = 2C/\tau_v$ and $K_{iv} = C\omega_{nv}^2$, where ω_{nv} is the outer loop natural frequency.

Damping coefficients $(r_d/L, r_q/L, r_{dc}/C)$ associated with classical PBC and the proposed UDE-PBC are set to $(1/\tau_i, 1/\tau_i, 1/10\tau_v)$ to get the desired closed-loop bandwidth. The filter parameters for the proposed controller can be selected 5–15 times of the current and DC link voltage controller bandwidths to obtain high disturbance rejection and fast tracking performance. However, due to the limitations of sampling frequency, the filter parameters cannot be selected to be too large. Besides, larger bandwidth will introduce high-frequency sensor noise. Therefore, taking into account the hardware capability and tracking response requirements, filter parameters $(R_{fd}, R_{fq}, R_{fdc})$ are set to $(5/\tau, 5/\tau, 1/2\tau)$ with trade-off between the convergence rate and dynamic response of the filter. The control parameters associated with the proposed and base controller are all given in Table II. It is shown in Fig. 8 that the measured three-phase grid currents and voltages in the stationary reference frame are transformed to the synchronous reference frame (SRF) by *abc-dq* transformation.

Ignoring zero sequence components and assuming that the grid voltages are balanced, the phase locked loop (PLL) scheme is designed such that the q-axis component of the grid voltages e_q is equal to zero with the help of simple PI controller which guarantees d-axis component is aligned with grid voltage. K_{pll} and T_{pll} are the PI parameters that are tuned so that the settling time is equal to 100 ms which are given in Table II.

TABLE II. CONTROL PARAMETERS.

UDE filter parameters $(\boldsymbol{R_{fd}, R_{fq}, R_{fdc}})$	(5000, 5000, 500)
Damping injection coefficients (r_1, r_2, r_3)	(6, 6, 0.01)
Time constants (τ_i, τ_v)	(0.001, 0.1)
Natural angular frequencies $(\omega_{ni}, \omega_{nv})$	(1000, 20)
Damping ratios (δ_i, δ_v)	(0.707, 0.707)
PLL Parameters $(\boldsymbol{K_{pll}, T_{pll}})$	(90, 0.0218)

A. Dynamic Performance of UDE-PBC

Figure 8 shows the dynamic response of the grid currents under the conditions with step change of the active and reactive powers for varied values of control gain $r_{d,q}$. Initially, the active power reference is set to 1 + j1 kVAr and kept at this value along the simulation, whereas the reactive power is suddenly changed from 1 kVAr to 0 kVAr and from 0 kVAr to -1 kVAr as shown in Fig. 9.

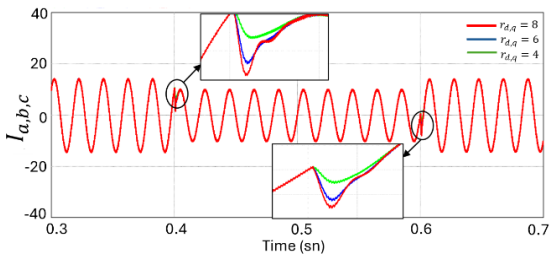

Fig. 8. Simulation results of UDE-PBC with different $r_{d,q}$ under step change of injected power.

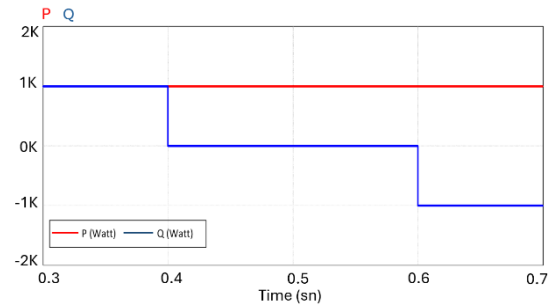

Fig. 9. Step change of active and reactive power reference.

It can be observed that, as the damping gains increase, the current dynamics has a faster transient response, and the tracking error decreases accordingly. Besides, increasing damping gains causes small overshoot. To compare the proposed scheme with the base controller, a set of results is given in Fig. 10. It can be observed that the proposed UDE-PBC strategy shows faster response and better tracking performance over the PI and PBC methods.

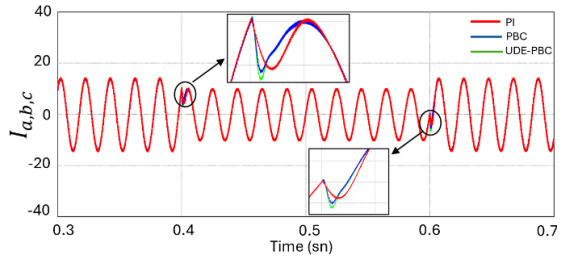

Fig. 10. Comparative simulation results of UDE-PBC, PI, PBC under step change of injected power.

B. *Control Performance of the UDE-PBC under Large Disturbance of Grid Voltage*

The performance of the proposed controller is tested under 50 % voltage sag of the grid and compared with classical PI and PBC approaches for different values of filter gains $R_{fd,q}$. The changes in grid voltages are shown in Fig. 11.

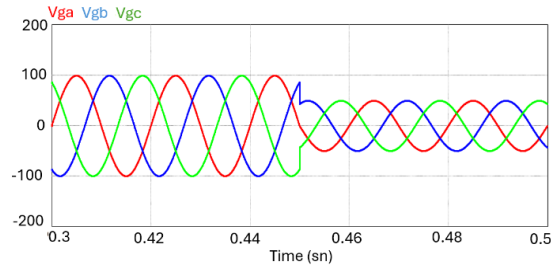

Fig. 11. Simulation waveforms of grid voltages under %50 voltage sag.

Figure 12 shows that the disturbance rejection performance becomes better when R_f increases for the proposed control method.

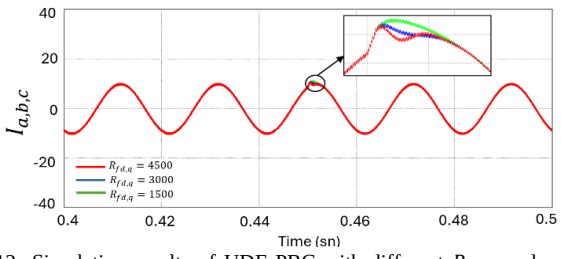

Fig. 12. Simulation results of UDE-PBC with different $R_{fd,q}$ under 50 % voltage sag.

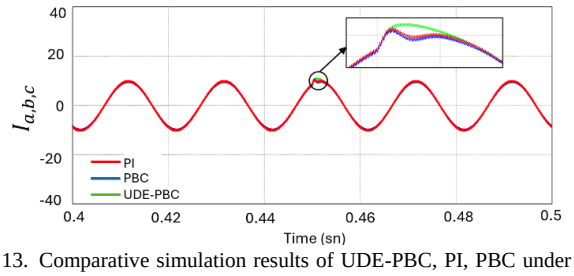

Fig. 13. Comparative simulation results of UDE-PBC, PI, PBC under step change in injected power.

As can be observed in Fig. 13, the base control method can operate under voltage sag disturbances. However, the PI method shows the slowest dynamic response. Compared to base controllers, faster dynamic response and lowest current THD are achieved with the UDE-PBC scheme.

V. EXPERIMENTAL WORK

A. *Dynamic Performance of the Proposed UDE-PBC*

In this section, the experimental results obtained to validate the performance of the proposed UDE-PBC during the step change of active and reactive power loads are presented.

Initially, active power reference is maintained as 1000 W, the reactive power reference was changed from 1000 VAr to 2000 Var (inductive load) and -1000 VAr (capacitive load) as shown in Figs. 14 and 15, respectively. It can be observed that the reference current, due to the step change of the reactive power, has a fast transient dynamics and low overshoot.

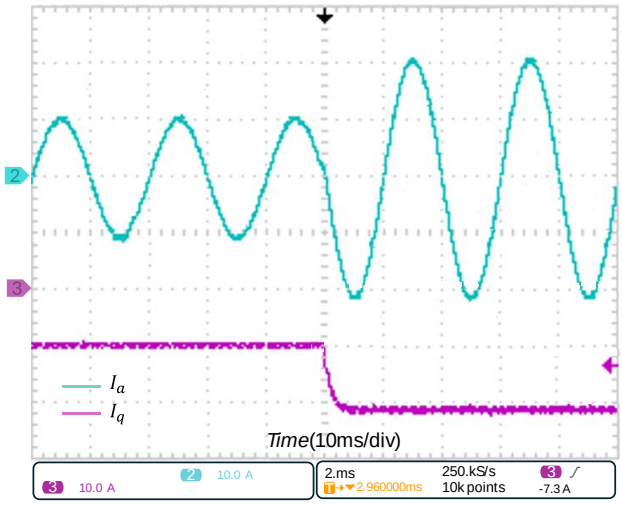

Fig. 14. Dynamic response of UDE-PBC under reactive power reference change from 1 kVar to 2 kVar.

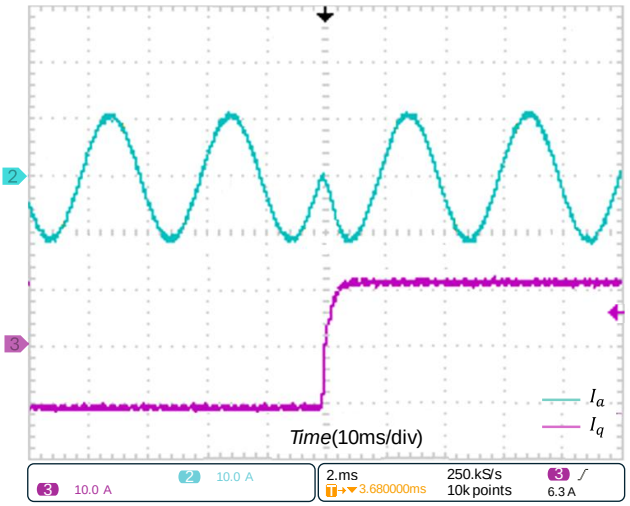

Fig. 15. Dynamic response of UDE-PBC under reactive power reference change from 1 kVar to -1 kVar.

B. *Control Performance under Parametric Mismatch*

To evaluate the robustness of the proposed UDE-PBC strategy, a set of comparative experiments with proportional-integral control and the classical PBC method under parameter mismatch was performed. The deviation of the parameters is handled by changing nominal parameters which are set in the programming code of controllers. Figures 16–

18 illustrate the responses of the base controller (PI, PBC) and the proposed UDE-PBC under r mismatch, respectively. Deviation progress is setting the filter inductor parameter as nominal value L_n and reducing filter resistor 50 % of nominal value r_n in the controller terms.

It can be observed from Fig. 17 that the performance of the conventional PBC strategy is deteriorated from the disturbance caused by the r parameter mismatch and there is a static error on the d-axis current. However, the PI control strategy can reach the reference current with zero steady-state error due to the integral part of the controller as shown in Fig. 16. Compared to Figs. 16 and 17, it is clear that UDE-PBC can achieve a more satisfactory transient performance as shown in Fig. 18. Parametric uncertainties are attenuated by low pass filter (LPF) and zero steady-state current tracking errors are achieved with the proposed controller.

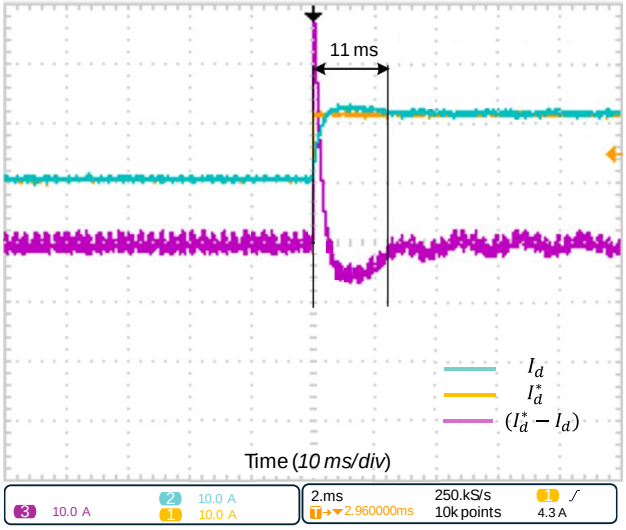

Fig. 16. Dynamic response of grid under parametric mismatch L = L_n and r = 50 % r_n for PI method.

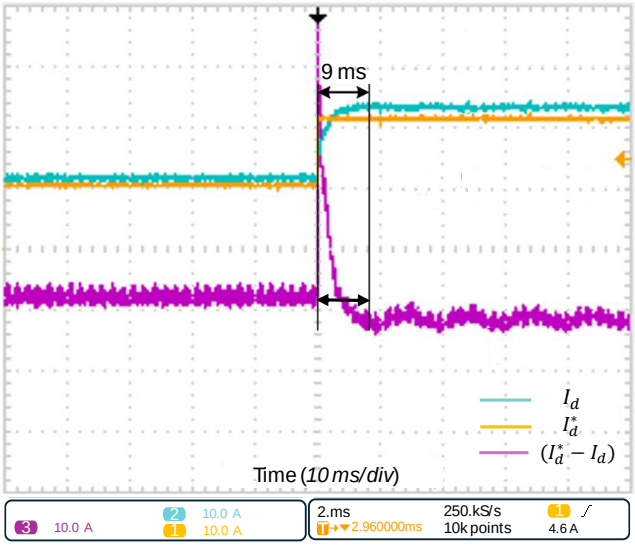

Fig. 17. Dynamic responses of the grid current under parametric mismatch L = L_n and r = 50 % r_n for passivity-based control.

In this section, of the experimental work, the DC link capacitance is set to C = 50 % C_n to examine the robustness performance of the proposed and baseline controllers on the DC link voltage regulation. Figures 19–21 show the results under step change of the grid current.

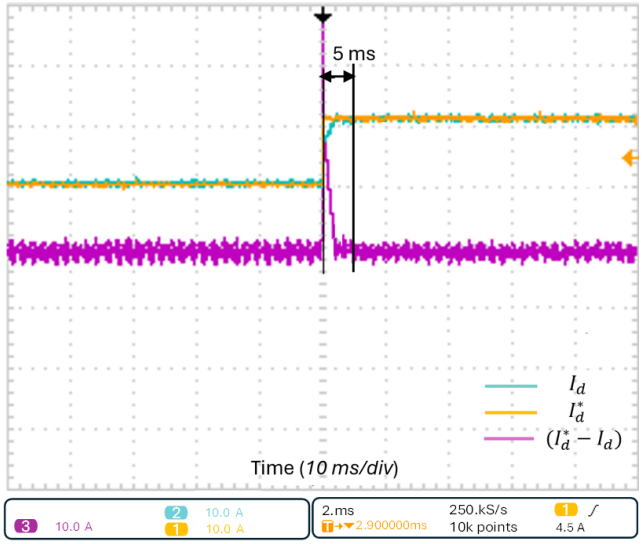

Fig. 18. Dynamic response of the grid under parametric mismatch L = L_n and r = 50 % r_n for UDE-PBC method.

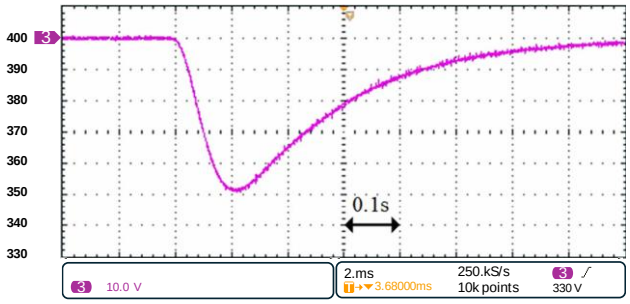

Fig. 19. Dynamic response of the DC link voltage for C = 50 % C_n and (r = r_n, L = L_n) for PI method.

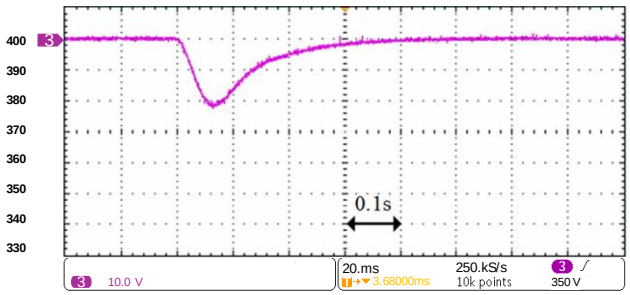

Fig. 20. Dynamic response of DC link voltage for C = 50 % C_n and (r = r_n, L = L_n) for passivity-based control.

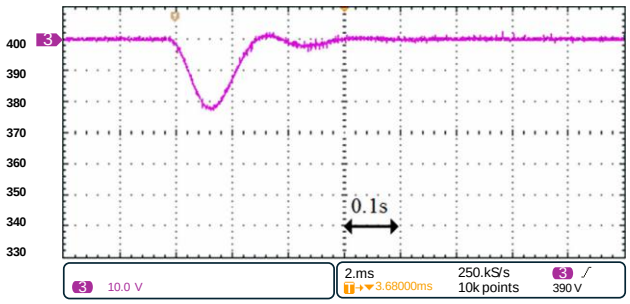

Fig. 21. Dynamic response of DC link voltage for C = 50 % C_n and (r = r_n, L = L_n) for UDE-PBC method.

It is observed that all three strategies can yield the DC link voltage regulation, and the variation of the DC link capacitance has little influence on the tracking error of the control system. By comparing Figs. 19 and 20, the dynamic response of the PBC controller is faster than that of the classical PI approach; however, the overshoot in the PI

controller is larger than that of the PBC strategy. From Fig. 21, it is seen that the proposed UDE-PBC provides the fastest dynamic performance as compared to the baseline methods and only little DC bus voltage fluctuation. The proposed control strategy needs less energy from the DC link capacitor.

Overall, it can be observed that the proposed UDE-PBC provides superior robustness to deal with the parametric uncertainties of the system and satisfactory recovery performance compared to the baseline controllers, which coincides with theoretical analysis.

VI. CONCLUSIONS

In this paper, a PBC strategy based on uncertainty and disturbance observer scheme was built for GTI to improve the robustness while achieving satisfactory dynamic performance. The complete port-controlled-Hamiltonian model of the GTI was developed. The proposed UDE-PBC method provides a composite control approach with the closed-loop response and uncertainties, which are considered as lumped disturbance. The design of the proposed control gains of UDE-PBC can be separated for the desired tracking response and disturbance bandwidth. In addition, computational and PWM delays have been taken into account during the construction of the closed-loop response. Compared with the PI and PBC, the UDE-PBC has good dynamic response and could reach the given references with zero tracking error under parametric variations. Finally, a 2-kW GTI prototype was used to verif[23y the UDE-PBC by comparative simulation and experimental results with PI and PBC.

CONFLICTS OF INTEREST

The authors declare that they have no conflicts of interest.

REFERENCES

[1] F. Blaabjerg, R. Teodorescu, M. Liserre, and A. V. Timbus, "Overview of control and grid synchronization for distributed power generation systems", *IEEE Transactions on Industrial Electronics*, vol. 53, no. 5, pp. 1398–1409, 2006. DOI: 10.1109/TIE.2006.881997.

[2] S. Vazquez, S. M. Lukic, E. Galvan, L. G. Franquelo, and J. M. Carrasco Solis, "Energy storage systems for transport and grid applications", *IEEE Transactions on Industrial Electronics*, vol. 57, no. 12, pp. 3881–3895, 2010. DOI: 10.1109/TIE.2010.2076414.

[3] D. Klimenta *et al.*, "Increasing the transmission performance of a conventional 110 kV cable line by combining a hydronic concrete pavement system with photovoltaic floor tiles", *Electrical Engineering*, vol. 103, no. 3, pp. 1401–1415, 2021. DOI: 10.1007/s00202-020-01167-4.

[4] F. Shi and J. Wang, "The HVDC supplementary control for AC/DC interconnected power grid based on Hamilton energy function theory", *Elektronika ir Elektrotechnika*, vol. 20, no. 4, pp. 15–21, 2014. DOI: 10.5755/j01.eee.20.4.4230.

[5] W.-K. Sou *et al.*, "A deadbeat current controller of LC-hybrid active power filter for power quality improvement", *IEEE Journal of Emerging and Selected Topics in Power Electronics*, vol. 8, no. 4, pp. 3891–3905, 2020. DOI: 10.1109/JESTPE.2019.2936397.

[6] Z. Liu, B. Zhang, K. Zhou, Y. Yang, and J. Wang, "Virtual variable sampling repetitive control of single-phase DC/AC PWM converters", *IEEE Journal of Emerging and Selected Topics in Power Electronics*, vol. 7, no. 3, pp. 1837–1845, 2019. DOI: 10.1109/JESTPE.2018.2862411.

[7] G. Bergna-Diaz, D. Zonetti, S. Sanchez, R. Ortega, and E. Tedeschi, "PI passivity-based control and performance analysis of MMC multiterminal HVDC systems", *IEEE Journal of Emerging and Selected Topics in Power Electronics*, vol. 7, no. 4, pp. 2453–2466, 2019. DOI: 10.1109/JESTPE.2018.2889152.

[8] R, Keskin, I, Aliskan, "Multi-Objective Optimisation-based Robust H∞ Controller Design Approach for a Multi-Level DC-DC Voltage Regulator", *Elektronika ir Elektrotechnika*, vol. 29, no. 1, pp. 4–14, 2023, DOI: 10.5755/j02.eie.32887.

[9] C. Zhang, X. Zhao, X. Wang, X. Chai, Z. Zhang, and X. Guo, "A grid synchronization PLL method based on mixed second- and third-order generalized integrator for DC offset elimination and frequency adaptability", *IEEE Journal of Emerging and Selected Topics in Power Electronics*, vol. 6, no. 3, pp. 1517–1526, 2018. DOI: 10.1109/JESTPE.2018.2810499.

[10] H. Feroura, F. Krim, B. Talbi, A. Laib, and A. Belaout, "Finite-set model predictive direct power control of grid connected current source inverter", *Elektronika ir Elektrotechnika*, vol. 23, no. 5, pp. 36–40, 2017. DOI: 10.5755/j01.eie.23.5.19240.

[11] M. Morawiec, "The adaptive backstepping control of permanent magnet synchronous motor supplied by current source inverter", *IEEE Transactions on Industrial Informatics*, vol. 9, no. 2, pp. 1047–1055, 2013. DOI: 10.1109/TII.2012.2223478.

[12] Z. Rymarski, K. Bernacki, and L. Dyga, "A control for an unbalanced 3-phase load in UPS systems", *Elektronika ir Elektrotechnika*, vol. 24, no. 4, pp. 27–31, 2018. DOI: 10.5755/j01.eie.24.4.21474.

[13] H. Komurcugil, "Improved passivity-based control method and its robustness analysis for single-phase uninterruptible power supply inverters", *IET Power Electronics*, vol. 8, no. 8, pp. 1558–1570, 2015. DOI: 10.1049/iet-pel.2014.0706.

[14] R. Ortega, A. J. Van der Schaft, I. Mareels, and B. Maschke, "Putting energy back in control", *IEEE Control Systems Magazine*, vol. 21, no. 2, pp. 18–33, 2001. DOI: 10.1109/37.915398.

[15] R. Ortega and E. Garcia-Canseco, "Interconnection and damping assignment passivity-based control: A survey", *European Journal of Control*, vol. 10, no. 5, pp. 432–450, 2004. DOI: 10.3166/ejc.10.432-450.

[16] R. Ortega, A. van der Schaft, F. Castanos, and A. Astolfi, "Control by interconnection and standard passivity-based control of Port-Hamiltonian systems", *IEEE Transactions on Automatic Control*, vol. 53, no. 11, pp. 2527–2542, 2008. DOI: 10.1109/TAC.2008.2006930.

[17] X. Lin and Y. Lei, "Coordinated control strategies for SMES-battery hybrid energy storage systems", *IEEE Access*, vol. 5, pp. 23452–23465, 2017. DOI: 10.1109/ACCESS.2017.2761889.

[18] J. Min, F. Ma, Q. Xu, Z. He, A. Luo, and A. Spina, "Analysis, design, and implementation of passivity-based control for multilevel railway power conditioner", *IEEE Transactions on Industrial Informatics*, vol. 14, no. 2, pp. 415–425, 2018. DOI: 10.1109/TII.2017.2747593.

[19] J. Lai, X. Yin, L. Jiang, X. Yin, Z. Wang, and Z. Ullah, "Disturbance-observer-based PBC for static synchronous compensator under system disturbances", *IEEE Transactions on Power Electronics*, vol. 34, no. 11, pp. 11467–11481, 2019. DOI: 10.1109/TPEL.2019.2900694.

[20] X. Li and X. Li, "Passivity-based control for movable multi-load inductively coupled power transfer system based on PCHD model", *IEEE Access*, vol. 8, pp. 100810–100823, 2020. DOI: 10.1109/ACCESS.2020.2997989.

[21] X. Guo, X. Liao, Q. Wang, Y. Wen, and T. Wu, "Designing active disturbance rejection control of permanent magnetic spherical actuator based on nonlinear extended state observer", *Elektronika ir Elektrotechnika*, vol. 28, no. 1, pp. 23–31, 2022. DOI: 10.5755/j02.eie.30102.

[22] R. Wang, B. Hu, S. Sun, F. Man, Z. Yu, and Q. Chen, "Linear active disturbance rejection control for DC side voltage of single-phase active power filters", *IEEE Access*, vol. 7, pp. 73095–73105, 2019. DOI: 10.1109/ACCESS.2019.2920626.

[23] M. Pastor and J. Dudrik, "Predictive control of grid-connected multilevel inverter with output LCL filter", *Elektronika ir Elektrotechnika*, vol. 21, no. 3, pp. 10–15, 2015. DOI: 10.5755/j01.eee.21.3.10033.

[24] Q.-C. Zhong and D. Rees, "Control of uncertain LTI systems based on an uncertainty and disturbance estimator", *Journal of Dynamic Systems, Measurement, and Control*, vol. 126, no. 4, pp. 905–910, 2004. DOI: 10.1115/1.1850529.

[25] J. Ren, Y. Ye, G. Xu, Q. Zhao, and M. Zhu, "Uncertainty-and-disturbance-estimator-based current control scheme for PMSM drives with a simple parameter tuning algorithm", *IEEE Transactions on Power Electronics*, vol. 32, no. 7, pp. 5712–5722, 2017. DOI: 10.1109/TPEL.2016.2607228.

[26] N. Alshek, S. Bronshtein, M. Elkayam, and A. Kuperman, "Modified uncertainty and disturbance estimator for enhanced periodic signals suppression", *IEEE Transactions on Industrial Electronics*, vol. 66, no. 2, pp. 1246–1254, 2019. DOI: 10.1109/TIE.2018.2833035.

[27] S. Y. Gadelovits, Q.-C. Zhong, V. Kadirkamanathan, and A. Kuperman, "Uncertainty and disturbance estimator-based controller equipped with a time-delayed filter to improve the voltage quality of inverters", *IEEE Transactions on Industrial Electronics*, vol. 66, no. 1, pp. 459–469, 2019. DOI: 10.1109/TIE.2018.2831182.

[28] Y. Ye and Y. Xiong, "UDE-based current control strategy for LCCL-type grid-tied inverters", *IEEE Transactions on Industrial Electronics*, vol. 65, no. 5, pp. 4061–4069, 2018. DOI: 10.1109/TIE.2017.2760850.

[29] Ü. A. Uslu, "Improved passivity based controller with nonlinear disturbance observer for grid tied voltage source inverters", Ph.D. dissertation, Dept. Elect. Eng., Gazi Univ., Ankara, Türkiye, 2019.